Photodissociation dynamics of the triiodide anion (I_3^-)

Hyeon Choi,[a] Ryan T. Bise, Alexandra A. Hoops, and Daniel M. Neumark
Department of Chemistry, University of California, Berkeley, California 94720
and Chemical Sciences Division, Lawrence Berkeley National Laboratory, Berkeley, California 94720

(Received 2 March 2000; accepted 10 May 2000)

The spectroscopy and dissociation dynamics of I_3^- were investigated using fast beam photofragment translational spectroscopy. The photofragment yield of I_3^- from 420 to 240 nm was measured, yielding two broadbands at the same energies as in the absorption spectrum of I_3^- in solution. Photodissociation dynamics measurements performed with two-particle time-and-position sensitive detection revealed two product mass channels having photofragment mass ratios of 1:2 and 1:1. Both channels were seen at all photolysis wavelengths. Translational energy distributions show that the 1:2 products are from a combination of $I(^2P_{3/2})+I_2^-$ and $I^*(^2P_{1/2})+I_2^-$. The 1:1 mass channel is from symmetric three-body dissociation to I^-+2I. © *2000 American Institute of Physics.* [S0021-9606(00)00730-3]

I. INTRODUCTION

The triiodide ion, I_3^-, is a well known chemical species with unusual properties. It is a classic example of a molecule that violates the octet rule. It is also one of relatively few closed-shell negative ions that has excited electronic states below its electron detachment threshold. During the last several years, there has been considerable interest in the time-resolved photodissociation dynamics of I_3^-. These experiments have been performed in polar solvents and in the gas phase, and yield markedly different results attributed to solvent effects on the short-time reaction dynamics. In order to better understand the differences between the two sets of results, more information on the gas phase dynamics is required. In this paper, we present a frequency-domain study of gas phase I_3^- photodissociation using fast beam photofragment translational spectroscopy.

The spectroscopy of triiodide ion (I_3^-) has been extensively studied in the condensed phase. Its electronic absorption spectrum is dominated by two broadbands centered at 290 and 360 nm,[1] henceforth referred to as the upper and lower bands. These bands are split approximately by the spin-orbit splitting of atomic I. While it is generally accepted[2] that the $\tilde{X}\,^1\Sigma_g^+$ ground state of I_3^- has the molecular orbital configuration $\cdots(\sigma_u)^2(\pi_u)^4(\sigma_g)^2(\pi_g)^4(\pi_u^*)^4(\sigma_u^*)^0$, assignment of the absorption spectrum has been controversial. The lower and upper bands were originally assigned as $\pi_g\rightarrow\sigma_u^*$ and $\sigma_g\rightarrow\sigma_u^*$ transitions with $^1\Pi_u$ and $^1\Sigma_u^+$ upper states, respectively, by Gabes *et al.*,[3,4] while Tasker[5] proposed a similar assignment with the energy ordering reversed. Mizuno *et al.*[6] pointed out that the lower band was too strong and had the wrong polarization dependence in crystalline CsI_3 to be a $\pi_g\rightarrow\sigma_u^*$ transition. They suggested that these two bands were from $\sigma_g\rightarrow\sigma_u^*$ transitions split by the spin-orbit coupling. This idea was considered more quantitatively in a semiempirical calculation including spin-orbit interaction by Okada *et al.*,[7] who assigned the two upper states as admixtures of $^3\Pi_{0+u}$ and $^1\Sigma_{0+u}$ states, both of which are 0^+ states in Hund case (c); the oscillator strength of both bands is due to the $^1\Sigma_{0+u}$ component, while the $^3\Pi_{0+u}$ component is mixed in by spin-orbit coupling. This assignment was supported by the electronic and magnetic circular dichroism spectra (MCD) of triiodide in solution by Isci and Mason.[8]

Early photodissociation studies of I_3^- in solution showed that excitation into either band produces diiodide ions I_2^-.[9–11] The resonance Raman spectrum of I_3^- reveals a long progression of the symmetric stretch, indicating that the initial motion on the excited state is along this coordinate.[12–14] Interest in I_3^- has been re-kindled by a series of femtosecond time-resolved transient absorption experiments used to study its photodissociation dynamics in solution. Banin *et al.*[15–20] excited the upper I_3^- band at 308 nm and observed coherent vibrational motion of I_2^- product anions in their $\tilde{X}\,^2\Sigma_u^+$ state. This coherent vibrational motion appears as early as 500 fs after the initial excitation, shows an average vibrational state of $\langle v\rangle=12$, and is irreversibly lost within 4 ps due to interaction with the solvent molecules. Using a similar technique, Kuhne *et al.*[21–23] measured the vibrational distribution and relative product yield of I_2^- at several wavelengths. They reported the product yield of I_2^- to be 1.0 at 400 nm (lower band) and 0.8 at 266 nm (blue edge of upper band), with the remainder assumed to be I^-+2I.

Experiments on gas phase I_3^- have begun only recently. Do *et al.*[24] measured the bond strength of I_3^- through collision-induced dissociation in a tandem mass spectrometer, obtaining a value of 1.31 ± 0.06 eV for dissociation to I_2+I^-. The photoelectron spectrum of I_3^- was taken by Taylor *et al.*[25] and the electron affinity of I_3^- was determined as 4.226 ± 0.013 eV. From these two experiments, one can construct the energy diagram for I_3^- photodissociation shown in Fig. 1.

Recently, Zanni *et al.*[26,27] studied the photodissociation of I_3^- in the gas phase using femtosecond photoelectron spectroscopy (FPES). In this study, I_2^- and I^- were found as

[a]Current address: Department of Chemistry and Biochemistry, University of California, Los Angeles, California 90095.

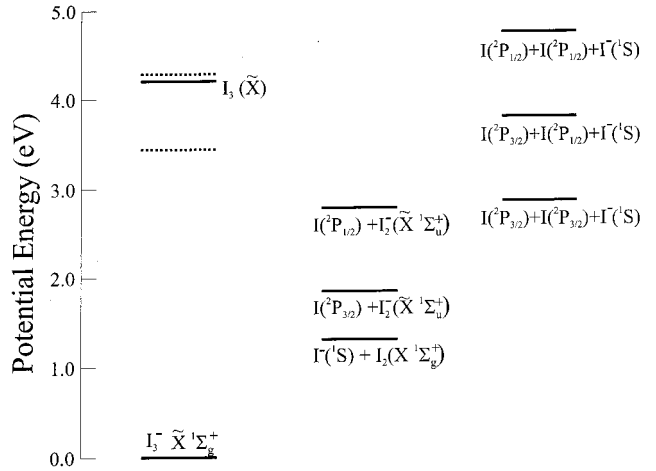

FIG. 1. Energetics of I_3^-. Electronic band maxima of I_3^- are shown as dotted lines.

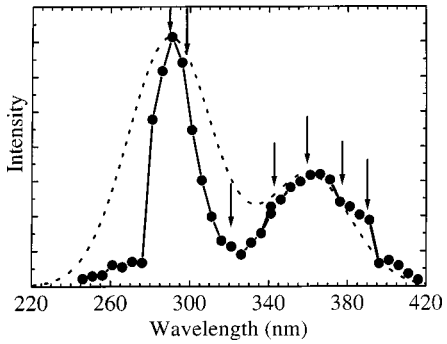

FIG. 2. Photofragment yield (PFY) spectrum of I_3^-. Solid line and circles: gas phase PFY spectrum. Dotted line: absorption spectrum of aqueous I_3^-.

photoproducts at 390 nm (lower band) with approximately equal yields. In addition, coherent vibrational motion of $I_2^-(\tilde{X})$ was observed and indicated much higher excitation ($\langle v\rangle = 67$) than in solution. To model the dynamics of this reaction, they constructed a potential energy surface that reproduced the vibrational energy distribution in quantum wave packet simulations. These calculations strongly implied that I^- was produced by three-body dissociation to $I^- + 2I$ rather than the lower energy $I_2 + I^-$ channel (see Fig. 1). Highly excited dihalide products have also been observed from the photodissociation of IBr_2^- and $BrICl^-$ in a recent study by Sanov *et al.*,[28] but no atomic halide product was seen.

A more complete study of I_3^- in the gas phase in needed to better understand the significant differences between the gas phase and solution results. Here, we present results using fast beam photofragment translational spectroscopy and probe several new aspects of the gas phase spectroscopy and dynamics. We are particularly interested in the following: First, the absorption spectrum of I_3^- in the gas phase has never been taken. Second, the photodissociation of gas phase I_3^- has not been studied at multiple photon energies. Third, experimental efforts on this reaction have been focused on detecting I_2^-, with no information about the spin-orbit state of the I photoproduct. The spin-orbit distribution would be very useful for understanding the correlation between the excited states of I_3^- and the photoproducts. Finally, while the work by Zanni *et al.*[26,27] provided indirect evidence that I^- production occurs via three-body dissociation, this mechanism can be assessed directly in the fast beam experiment.

II. EXPERIMENT

Photodissociation of the triiodide anions (I_3^-) was studied using our fast beam photofragment spectrometer.[29–31] This instrument is generally used for neutral free radical dissociation but can also be applied to negative ion photodissociation. To make I_3^-, argon gas (3 psig) is flowed over iodine crystals (I_2) at room temperature. The resulting mixture supersonically expands through a pulsed valve into the source region of the apparatus. Anions are generated by crossing the free jet with a 1 keV electron beam just downstream of the valve orifice. Rotational temperatures of 20–50 K are typically attained in the course of the expansion.

The pulsed molecular beam passes through a skimmer into a differentially pumped region. Negative ions in the beam are accelerated to 8 keV and mass selected with a collinear time-of-flight (TOF) mass spectrometer. The I_3^- ion packet is intersected by a linearly polarized excimer-pumped pulsed dye laser beam and some I_3^- ions absorb a photon and dissociate. The photofragments are detected by a multichannel plate detector lying either 1 or 2 m downstream from the dissociation region. A blocking strip across the center of the detector prevents parent molecules from reaching the detector, whereas photofragments with sufficient recoil energy miss the beam block and strike the detector. These fragments are generally detected with high efficiency (up to 50%) due to their high laboratory kinetic energy.

Two types of experiments are performed to characterize the photodissociation of I_3^-. First, the photofragment yield (PFY) spectrum is obtained by collecting the total flux of fragments as a function of the photodissociation laser wavelength. To investigate the photodissociation dynamics at a fixed wavelength, two photofragments from a parent molecule are collected in coincidence using a time- and position-sensitive detector. In this experiment, we measure the distance R between the two fragments on the detector, their arrival time difference τ, and the individual displacement of the two fragments, r_1 and r_2, from the detector center for each dissociation event. From these we obtain the center-of-mass translational energy E_T, the scattering angle with respect to laser polarization, θ, and the photofragment mass ratio m_1/m_2 via

$$\frac{m_1}{m_2} = \frac{r_2}{r_1}, \tag{1}$$

$$\theta = \tan^{-1}\left(\frac{R}{v_0 \cdot \tau}\right), \tag{2}$$

$$E_T \cong E_0 \cdot \frac{\mu}{M} \cdot \frac{(v_0 \cdot \tau)^2 + R^2}{l^2}. \tag{3}$$

Here E_0 and v_0 are the ion beam energy and velocity, respectively, μ is the reduced mass, and l is the flight length

from the photodissociation region to the detector. Although the relative recoil distance R is determined with high precision ($R/\Delta R \approx 100$), the individual recoil distance r_1 and r_2 are less precisely determined due the finite size of the parent beam, resulting in mass resolution $m/\Delta m \approx 10$. The energy resolution ($\Delta E_T/E_T$) under the conditions in these studies is around 2%.

There are some issues is performing these experiments on I_3^- that are absent in our studies of neutral free radical dissociation. The dynamics experiment requires that two fragments be detected in coincidence. The front of the detector is biased at a high negative potential, so only neutral fragments can be detected. This might seem problematic for I_3^- photodissociation, because one of the photoproducts will be an ion. However, the dissociation laser photon energy is always greater than the electron affinity of either I or I_2 (3.059[32] and 2.524 eV,[33] respectively), so the dissociation laser can detach I^- and I_2^- photoproducts, creating neutrals that are then detected. The possible role of three-body dissociation is an additional complication, since the coincidence detector can only process two events per laser shot. In fact, as discussed in more detail in Secs. III B and IV, the situation often arises in which only two out of the three fragments reach the detector, so this channel can still be treated properly.

III. RESULTS AND ANALYSIS

A. Photofragment yield (PFY) spectrum

The PFY spectrum of I_3 from 416 to 246 nm, shown as the solid line with circles in Fig. 2, was acquired with a step size of 5 nm. Each point was obtained at the same laser fluence (50 mJ/cm^2) and the same parent ion density. The spectrum is covered using 11 different laser dyes.

The PFY spectrum shows two intense features around 360 nm and 290 nm. These maxima agree well with the absorption spectrum of aqueous I_3^-,[7] shown as a dotted line in Fig. 2, as does the band profile for the lower band. However, the upper band in the PFY spectrum is noticeably narrower than in the absorption spectrum. This difference might be caused by photodetachment of I_3^-, energetically possible below 293 nm,[25] since this would deplete the PFY signal. On the other hand, the upper band on the PFY spectrum is narrower to the red of the band maximum as well, indicating a real difference in peak widths in gas phase and solution.

B. Photodissociation dynamics of I_3^-

1. Photofragment mass ratio (m_1/m_2)

Photodissociation dynamics experiments were performed at selected photon energies marked by arrows in Fig. 2. Data at 3.18 and 3.31 eV were taken at a flight length of 2 m, and all higher energy data were obtained with a flight length of 1 m; these flight lengths were chosen to optimize collection of the low and high energy photofragments.

The first information we get from this experiment is the ratio of the fragment masses, shown in Fig. 3 at 3.87 eV (320 nm). It is immediately seen that there are two product channels occurring at this photon energy with mass ratios of 1:2 and 1:1. The peaks are somewhat broader than expected based on our typical photofragment mass resolution ($m/\Delta m \approx 10$), possibly reflecting some of the complicated dissociation dynamics discussed below. At every photon energy we probed, a similar product mass ratio is obtained.

As shown in Fig. 1, there are several product channels that are thermodynamically feasible following UV excitation of I_3^-:

$$
\begin{aligned}
I_3^-(\tilde{X}) + h\nu_{\text{photon}} \rightarrow I^-(^1S) + I_2(\tilde{X}) \qquad & D_0 = 1.31 \pm 0.06 \text{ eV (channel 1)} \\
I(^2P_{3/2}) + I_2^-(\tilde{X}) \qquad & 1.85 \pm 0.06 \text{ eV (channel 2)} \\
I^*(^2P_{1/2}) + I_2^-(\tilde{X}) \qquad & 2.79 \pm 0.06 \text{ eV (channel 3)} \\
I(^2P_{3/2}) + I(^2P_{3/2}) + I^-(^1S) \qquad & 2.85 \pm 0.06 \text{ eV (channel 4)} \\
I(^2P_{3/2}) + I^*(^2P_{1/2}) + I^-(^1S) \qquad & 3.80 \pm 0.06 \text{ eV (channel 5).}
\end{aligned}
$$

The energetics are based on the bond strength (1.31 ± 0.06 eV) of I_3^- from the collision-induced dissociation experiment by Do *et al.*,[24] the spin-orbit coupling constant for the I atom (0.943 eV), and the dissociation energies of I_2(1.542 eV)[34] and I_2^-(1.007 eV).[33] In addition to the above channels, the low-lying excited states of I_2 ($\tilde{A}'\,^3\Pi_{2u}$ and $\tilde{A}\,^3\Pi_{1u}$)[35] and I_2^- ($\tilde{A}$ or $\tilde{A}'\,^2\Pi_g$)[36,37] are also accessible at excitation energies used here. However, we cannot distinguish these I_2 and I_2^- states from vibrationally excited I_2^- in the $\tilde{X}$ state.

Channels 1–3 are two-body dissociation channels that are possible candidates for the products with 1:2 mass ratios, while channels 4–5 are three-body dissociation channels. Three-body dissociation of I_3^- can occur within two limits: symmetric and asymmetric dissociation. In symmetric dissociation, the two bond lengths increase at the same rate as the dissociation proceeds, whereas in asymmetric dissociation the two bond cleavage events are distinct, in the sense that the diatomic fragment persists for at least one vibrational period. Our observation of photofragments with a 1:1 mass ratio is a strong indication for symmetric three-body dissociation. In this limit, the two end atoms fly apart and the central atom remains stationary in the center-of-mass frame. Thus the central atom follows the same trajectory as the par-

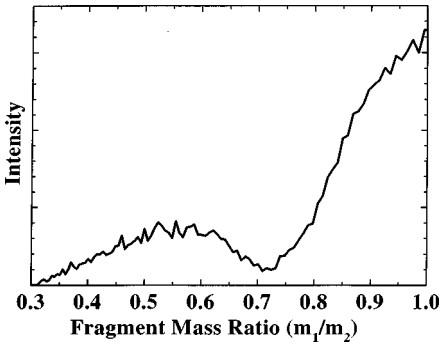

FIG. 3. Photofragment mass ratio (m_1/m_2) of I_3^- at photon energy 3.64 eV (341 nm).

ent molecule and hits the beam block in front of detector, whereas the two end atoms are detected with equal displacement from the center of the detector [i.e., $r_1=r_2$ in Eq. (1)].

2. Energy and angular distributions

For each channel, the joint translational energy and angular distribution is given by

$$P(E_T,\theta)=P(E_T)\cdot(1+\beta(E_T)\cdot P_2(\cos(\theta))), \tag{4}$$

in which $\beta(E_T)$ is the anisotropy parameter. For the channel with the 1:1 mass ratio, $\mu=1/2\cdot m_I$ (m_I=mass of I atom) is used in Eq. (3).

The limiting cases of $\sin^2\theta$ and $\cos^2\theta$ angular distributions are given by $\beta=-1$ and $+2$, respectively. Generally speaking, a parallel transition shows a positive β parameter while $\beta<0$ for a perpendicular transition. Both mass channels show a positive β parameter in agreement with the observation of a parallel transition in (xanthotoxin)$\cdot KI_3$ crystal by Mizuno *et al.*[6] However, accurate measurement of the β parameter is hampered because the beam block allows detection over a very restricted angular range.

$P(E_T)$ distributions for the 1:2 mass channel from I_3^- dissociation are shown in Fig. 4. Distributions associated with transitions to the lower and the upper bands are shown on the left and right sides of Fig. 4, respectively. The $P(E_T)$ distributions show two main features at every photon energy labeled as A and B in Fig. 4. Both features move toward higher E_T with increasing photon energy.

Channels 1–3 all correspond to products with a mass ratio of 1:2. With our detection scheme, we cannot distinguish between I^-+I_2 and $I+I_2^-$ products. However, at all excitation energies studied here, no products are seen at energies above the maximum allowed for channel 2 (rightmost arrows in Fig. 4). We therefore attribute all products in Fig. 4 to channels $2(I+I_2^-)$ and $3(I^*+I_2^-)$. The two brackets in each plot show the maximum and minimum translational energy for the two channels; at energies below the minimum, the I_2^- internal energy would exceed its bond dissociation energy and it would dissociate long before reaching the detector. Features A and B always fall within the allowed range for channels 2 and 3, respectively, so feature A is assigned to channel 2 and feature B to channel 3. For all excitation energies in the lower band, feature A drops abruptly at the translational energy corresponding to the opening of channel 3.

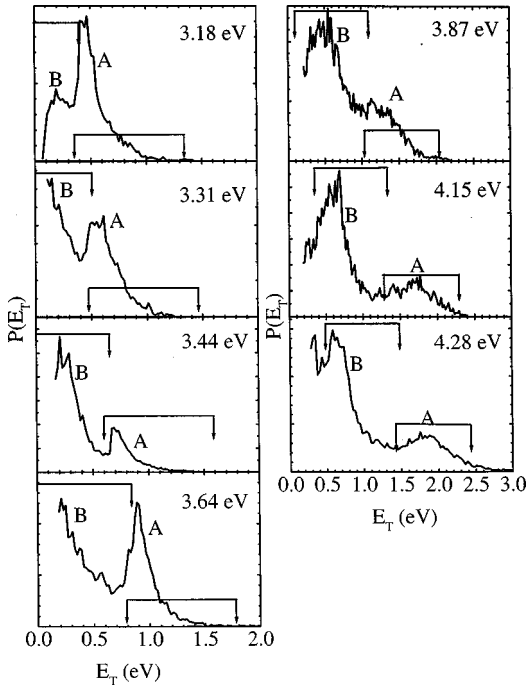

FIG. 4. Translational energy $P(E_T)$ distributions of I_3^- with 1:2 mass ratio at selected photon energies. Brackets indicate maximum and minimum translational energies for channels 2 and 3 (see text).

With these assignments, average internal excitation energies of the I_2^- product for both channels ($\langle E_{\text{int}}\rangle$) are obtained by

$$\langle E_{\text{int}}\rangle = h\nu_{\text{photon}} - D_0 - \langle E_T\rangle, \tag{5}$$

where $h\nu_{\text{photon}}$ and D_0 are photon energy and dissociation energy for each channel. The average translational energy ($\langle E_T\rangle$) for each channel is obtained by averaging the $P(E_T)$ over the allowed translational energy range (i.e., within the brackets in Fig. 4). Values of $\langle E_{\text{int}}\rangle$ at each photolysis energy are given in Table I.

The internal energy of the I_2^- can be partitioned between vibration and rotation. Since I_3^- is linear in its ground and excited states, we expect relatively little product rotational energy. $\langle E_{\text{int}}\rangle$ can then be converted into a reasonably accurate upper bound on $\langle v\rangle$ for the I_2^- product through:

$$\langle E_{\text{int}}\rangle = \omega_c\cdot\langle v\rangle - \omega_e\chi_e\cdot(\langle v\rangle+\tfrac{1}{2})^2+\tfrac{1}{4}\cdot\omega_e\chi_e\,. \tag{6}$$

TABLE I. Summary for 1:2 mass channel.

	$\langle E_{\text{int}}\rangle$ (eV)		$\langle v\rangle$		Branching ratio
$h\nu_{\text{photon}}$	Channel 2	Channel 3	Channel 2	Channel 3	Channel 2/3
3.18 eV	0.79	0.19	79	15	2.62
3.31 eV	0.81	0.33	83	27	0.97
3.44 eV	0.80	0.39	81	32	0.37
3.64 eV	0.82	0.53	84	46	0.72
3.87 eV	0.69	0.53	65	46	0.37
4.15 eV	0.58	0.68	52	64	0.33
4.28 eV	0.58	0.69	52	65	0.41

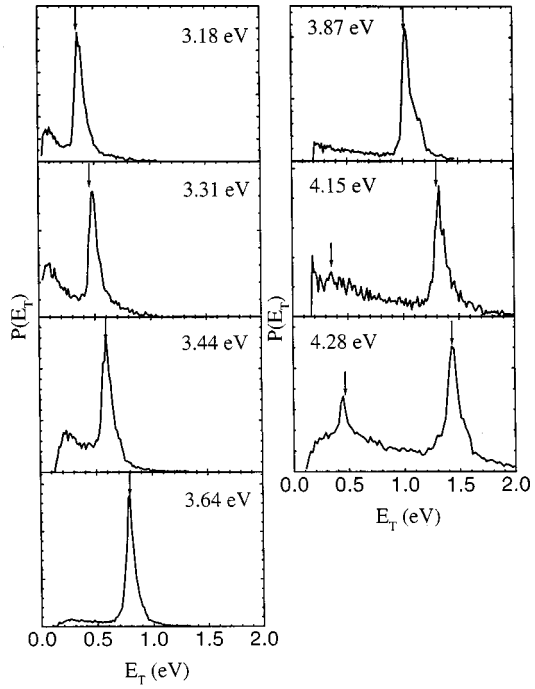

FIG. 5. Translational energy $P(E_T)$ distributions of I_3^- with 1:1 mass ratio at selected photon energies. Arrows indicate expected translational energy for symmetric three-body dissociation.

In Eq. (6), the vibrational frequency (ω_e) and anharmonicity ($\omega_e\chi_e$) of I_2^- are 110 and 0.370 cm^{-1}, respectively, as determined from the photoelectron spectra of Zanni *et al.*[33] The values $\langle v\rangle$ at each photolysis energy are also summarized in Table I. In addition, we calculate the branching ratio, channel 2/3, in Table I by integrating features A and B in each $P(E_T)$ distribution. The very small energy overlap between these features will not affect this calculation significantly. However, the I_2^- ions must be photodetached prior to the detector, as discussed in Sec. II, and we assume the photodetachment efficiency of the I_2^- product is independent of its excitation energy. Under this assumption, the population of highly vibrationally excited $I_2^-(v>80)$ is underestimated due to the poor Franck–Condon overlap between those states and the bound states of I_2. Although this correction can be calculated for each vibrational state, we have not done so since individual product vibrational levels are not resolved.

Table I indicates the trends in $\langle v\rangle$ as a function of photon energy. For channel 3, $\langle v\rangle$ increases with $h\nu$ over the full range of excitation energies, indicating that energy conservation is controlling the extent of I_2^- vibrational excitation. For channel 2, $\langle v\rangle$ is approximately constant throughout the lower band and drops once the upper band is accessed. The branching ratio (channel 2:3) decreases with increasing $h\nu$ throughout the lower absorption band except at 3.64 eV, while it remains around 0.3–0.4 throughout the upper band.

$P(E_T)$ distributions for the 1:1 mass channel are shown in Fig. 5. These distributions are dominated by one or (at $h\nu=4.28$ eV) two sharp peaks, and also show broader, generally less intense features at lower E_T than the sharp peaks. As discussed in Sec. III B, the observation of a 1:1 product mass channel strongly suggests symmetric three-body dissociation to $I+I+I^-$. In the symmetric limit, the central atom is stationary, and the relative translational energy of the two end atoms is fixed at $E_T=h\nu-D_0$, where D_0 is the threshold energy for channel 4 or 5. The arrows in Fig. 5 show these values of E_T, and in all cases the arrows match the positions of the sharp peaks in the $P(E_T)$ distributions, confirming that these features are from symmetric three-body dissociation. All peaks correspond to $I+I+I^-$ except for the peak at lower E_T at $h\nu=4.28$ eV, which corresponds to $I+I^*+I^-$. The latter channel is accessible at $h\nu=4.15$ eV but is not observed at that energy.

TABLE II. Branching ratios I_3^- photodissociation into the two mass channels (unit: %).

$h\nu_{photon}$	1:2 mass channel	1:1 mass channel
3.18 eV	47	53
3.31 eV	57	43
3.44 eV	67	33
3.64 eV	55	45
3.87 eV	59	41
4.15 eV	52	48
4.28 eV	45	55

While the sharp peaks in Fig. 5 correspond to the appropriate kinetic energies for symmetric three-body dissociation, we note that (a) the peaks are considerably broader than the experimental kinetic energy resolution, ~150 meV vs ~20 meV, and (b) there are broad features in addition to the sharp peaks. The origin of these two aspects of the $P(E_T)$ distributions is considered in the next section.

Finally, we analyze the branching ratio of two-body versus three-body dissociation in Table II by integrating the $P(E_T)$ distributions in Figs. 4 and 5. Three-body dissociation decreases in the lower band with increasing $h\nu$ except at 3.64 eV, following the same trend as the channel 2/3 branching ratio. In the upper band, the three-body channels become more intense with increasing $h\nu$.

IV. CLASSICAL TRAJECTORY CALCULATIONS

To gain further insight into the three-body dissociation dynamics, classical trajectory calculations were performed on a collinear model LEPS excited state potential energy surface for I_3^-. This potential energy surface, the parameters of which are given in Table III, was previously used for wave packet simulations by Zanni *et al.*[27] and is plotted in Fig. 6. (Note that some of the previously published parameters were not labeled correctly.[27]) It differs from a previously published LEPS surface by Benjamin *et al.*[38] in that it has a shallow well in the transition state region; this was found necessary to reproduce the I_2^- vibrational energy distribution seen by Zanni *et al.* Trajectories were computed by standard methods.[39,40] Numerical integration of Hamilton's equations was performed using the sixth-order Gear method with variable step size. Initial conditions were selected by projecting the zero-point symmetric and asymmetric stretching motion of I_3^- onto the excited state surface. We are there-

TABLE III. Parameters for the potential energy surface ($I^{r_{ab}}I^{r_{bc}}I$).

Ground state potential surface for I_3^-
$V_g(Q_1,Q_3)=\frac{1}{2}\mu_1\omega_1^2(Q_1-Q_{\rm eq})^2+\frac{1}{2}\mu_2\omega_2^2Q_3^2$
$Q_1=r_{ab}+r_{bc}\quad Q_3=r_{ab}-r_{bc}$
$\omega_1^a=112\ {\rm cm}^{-1}\quad \omega_2^b=145\ {\rm cm}^{-1}\quad Q_{\rm eq}=5.358$ Å $\quad \mu_1=63.5$ amu $\quad \mu_3=21.2$ amu
Excited state potential surface for I_3^-
$V_e(r_{ab},r_{bc},r_{ac})=\Delta E_0+Q_{ab}+Q_{bc}+Q_{ca}-(J_{ab}^2+J_{bc}^2+J_{ca}^2-J_{ab}J_{bc}-J_{bc}J_{ca}-J_{ca}J_{ab})^{1/2}$
$Q_{\alpha\beta}=\frac{[(1+S_{\alpha\beta})^1E(r_{\alpha\beta})+(1-S_{\alpha\beta})^3E(r_{\alpha\beta})]}{2(1+S_{\alpha\beta})}\quad {}^1E(r_{\alpha\beta})=D_{\alpha\beta}[1-e^{-\beta_{\alpha\beta}(r_{\alpha\beta}-r_{\alpha\beta}^{eq})}]^2-D_{\alpha\beta}$
$J_{\alpha\beta}=\frac{[(1+S_{\alpha\beta})^1E(r_{\alpha\beta})-(1-S_{\alpha\beta})^3E(r_{\alpha\beta})]}{2(1+S_{\alpha\beta})}\quad {}^3E(r_{\alpha\beta})=\{D_{\alpha\beta}[1+e^{-\beta_{\alpha\beta}(r_{\alpha\beta}-r_{\alpha\beta}^{eq})}]^2-D_{\alpha\beta}\}/2$
$r_{ab}^{eq}=r_{bc}^{eq}=3.205$ Å $\quad D_{ab}=D_{bc}=1.014$ eV $\quad \beta_{ab}=\beta_{bc}=1.181\ {\rm Å}^{-1}\quad S_{ab}=S_{bc}=0.50$
$r_{ca}^{eq}=2.983$ Å $\quad D_{cu}=1.010$ eV $\quad \beta_{ca}=1.000\ {\rm Å}^{-1}\quad S_{ca}=0.00$
$\Delta E_0=2.890$ eV

fore sampling a range of excitation energies determined by the Franck–Condon overlap between the ground and excited state surfaces.

A total of 1764 trajectories were run, of which 70 produced three-body dissociation. Several sample trajectories leading to three-body dissociation are shown in Fig. 6. In all of these, the trajectories follow the symmetric stretch quite closely until adjacent I atoms are separated by ~6 Å, after which they begin to spread along the antisymmetric stretch coordinate. No trajectories which reach the repulsive walls in the I_2^- product valleys lead to three-body dissociation in this calculation. Trajectories of this type would represent asymmetric three-body dissociation, so it appears that this process does not occur.

We next consider how the products from the trajectories in Fig. 6 map onto the two-particle position-sensing detector in our experiment. The positions of the three atoms at the detector are obtained from the asymptotic velocities of the three I atoms and the flight time (~31 μs) to the detector at an ion beam energy of 8 keV and flight length of 2 m. For each trajectory, all initial orientations of the molecular axis relative to the ion beam axis are considered. We find two classes of trajectories, shown with solid and dotted lines in Fig. 6. For the solid trajectories, the central atom is blocked by the beam block (8 mm wide) and the two end atoms are detected. These trajectories are detected as products with a 1:1 mass ratio and correspond to the sharp peaks seen in the experimental $P(E_T)$ distributions. However, even these trajectories show some displacement along the antisymmetric stretch coordinate, resulting in a slight energy broadening of the peaks, and this agrees with what is seen experimentally.

For the trajectories shown with dotted lines, there are at least some initial orientations for which the central atom will miss the beam block, resulting in three atoms hitting the detector. Simulations of the detector output under these conditions suggest that these types of trajectories are responsible for the broad features at low E_T seen in Fig. 5.

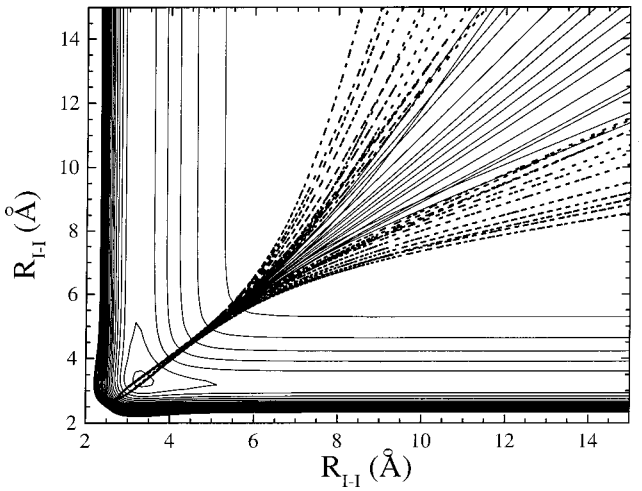

FIG. 6. Classical trajectories leading to symmetric three-body dissociation of I_3^- on potential energy surface. See text for explanation of solid and dotted lines.

V. DISCUSSION

A. PFY spectrum

The PFY spectrum in Fig. 2 is equivalent to the gas phase absorption spectrum of I_3^- in the limit that the quantum yield for photodissociation is unity. This limit should hold for wavelengths above 293 nm; at lower wavelengths, photodetachment as well as photodissociation can occur. The competition between the two processes cannot be assessed in our experiment. However, the I_3^- photoelectron spectrum shows a much stronger photodetachment transition to a low-lying excited state of I_3 lying about 0.26 eV above the ground state.[25] Detachment to this excited state is accessible at wavelengths below 280 nm, which coincides with the very abrupt drop in the PFY intensity in Fig. 2, so it is likely that photodetachment competes effectively with photodissociation at least below 280 nm.

Both bands in the gas phase PFY spectrum show a positive value of β, the photofragment anisotropy parameter, indicating they are parallel transitions. This is consistent with consistent with their assignment[7,8] to transitions to spin-orbit induced admixtures of the ${}^1\Sigma_{0+u}$ and ${}^3\Pi_{0+u}$ states, with the oscillator strength coming from the ${}^1\Sigma_{0+u}$ component. The upper band is clearly narrower than the lower band, even

taking into account the possibility of photodetachment competing with photodissociation below 293 nm, because the upper band is narrower on both sides of its maximum at 290 nm. The two band maxima in the gas phase PFY spectra agree with the absorption maxima in solution. While the width of the lower band is the same in gas phase and solution, the upper band is narrower in the gas phase PFY spectrum. This difference between the bands is most likely not a temperature effect; recent work in ethanol solution[41] shows that both bands narrow slightly as the temperature is lowered from 300 to 135 K.

The narrower upper band in the gas phase spectrum could simply arise from Franck–Condon effects, such as a lesser slope along the symmetric stretch coordinate in the Franck–Condon region for the excited state potential energy surface. On the other hand, it is possible that the lower band is composed of two overlapping electronic transitions. Analysis of the magnetic circular dichroism spectrum of Isci and Mason[8] indicates there is a state with predominantly $^1\Pi_u$ character at 343 nm (3.61 eV). A transition to this state is symmetry allowed but expected to be weak. While there is no direct evidence from our spectra for this state, we note that the two-body and three-body $P(E_T)$ distributions at 3.64 eV are quite different from those slightly higher and lower in energy; feature A (i.e., channel 2) is unusually large in the two-body distribution, and the sharp peak in the three-body distribution is particularly distinct. Both of these effects suggest some dissociation occurs on a different upper state surface than at neighboring excitation energies.

B. Photodissociation dynamics of I_3^-

The separation of the two electronic bands of I_3^- is close to the spin-orbit splitting in atomic iodine. Based on this, it was suggested that the excited states responsible for the lower and upper bands correlate to the asymptotic channels $I_2^- + I(^2P_{3/2})$ and $I_2^- + I^*(^2P_{1/2})$, respectively.[42,43] This correlation has also been implicit in quantum dynamical simulations of I_3^- photodissociation, in which dissociation was assumed to occur on a single surface correlation to one of these asymptotes.[17,22,27,38] Our results clearly show this to be an oversimplification; the $P(E_T)$ distributions in Fig. 4 show that both channels are populated regardless of which electronic band is excited. Tasker[5] proposed that the lower band was a $^1\Sigma_u$ state correlating to $I_2^- + I^*(^2P_{1/2})$, and the upper band a $^1\Pi_u$ state correlating to $I_2^-(^2\Pi_g) + I(^2P_{3/2})$. This assignment of the upper states is at variance with the accepted assignment discussed in the Introduction and the previous section, and the proposed atomic iodine correlations do not agree with the experimental results. In addition, since the $I_2^-(^2\Pi_g)$ excited states are very weakly bound,[44,45] one would expect significant asymmetric three-body dissociation on a potential energy surface correlating to $I_2^-(^2\Pi_g) + I(^2P_{3/2})$. We observe about the same degree of three-body dissociation from both electronic bands, and this process appears to be symmetric rather than asymmetric.

The presence of both two-body channels (channels 2 and 3) as well as three-body dissociation at all wavelengths strongly suggests that the dissociation dynamics are nonadiabatic and involve curve crossings between the upper states responsible for the I_3^- absorption spectrum. Nonetheless, the data for the lower band (for $h\nu < 3.64$ eV) show an interesting correlation that provides some insight into the dissociation dynamics. As the photon energy is increased from 3.18 to 3.44 eV, production of $I_2^- + I^*$ increases at the expense of $I_2^- + I$ and three-body dissociation (see Tables I and II). Thus in this energy range, channels 2 and 4 track one another, suggesting that they result from dissociation on the same potential energy surface, while dissociation on a different surface correlating to channel 3 becomes favored as the photon energy is raised.

Regardless of which two-body channel is formed, substantial I_2^- vibrational excitation is generally observed, which is by and large consistent with our previous gas phase femtosecond photoelectron spectroscopy study.[27] In that work, excitation at 390 nm resulted in coherently vibrating I_2^- photoproducts with $\langle v \rangle = 67$, or 0.70 eV of vibrational energy. Our results at 390 nm (3.18 eV) yield an upper bound of $\langle v \rangle = 79$, or 0.79 eV vibrational energy for channel 2. For channel 3, the degree of I_2^- vibrational excitation is much less at this photon energy ($\langle v \rangle = 15$ is the upper bound) reflecting conservation of total energy. The FPES experiment showed no evidence for I_2^- with low vibrational energy. The source of this discrepancy could be that channel 3 is relatively minor at 3.18 eV.

In contrast to the gas phase work, transient absorption spectroscopy studies on I_3^- photodissociation in solution show evidence for much less I_2^- vibrational excitation even at the shortest observation times (300–500 fs). For example, photodissociation of I_3^- in ethanol at 400 nm[21] resulted in an I_2^- vibrational distribution with $\langle v \rangle = 14$ at the earliest observation times. The earlier work by Ruhman and co-workers[16] at 308 nm (upper band, 4.03 eV) yielded a similarly low value, $\langle v \rangle = 12$. Our $P(E_T)$ distribution at 4.15 eV shows that channel 3 dominates in the gas phase, and that $\langle v \rangle$ for channels 3 and 2 is significantly higher than the solution result (upper bounds of 64 and 52, respectively). Hence, the observation of considerably greater I_2^- vibrational excitation in the gas phase experiments appears to be independent of photon energy. In addition, while we observe substantial three-body dissociation at all wavelengths, no I^- production occurs in solution except as a minor channel at 266 nm.[22] Overall, the influence of solvent effects on the I_3^- photodissociation dynamics is prominent throughout the entire UV absorption spectrum; possible origins of these effects have been discussed elsewhere.[27]

We close by considering the three-body dissociation channels in more detail. The lowest energy three-body channel (channel 4) is observed at all photon energies investigated here. Channel 5 ($I + I^* + I^-$) is not seen until 4.28 eV, even though it becomes open at 3.80 eV. The sharp peak in the $P(E_T)$ distribution shows that channel 5 is also a symmetric three-body channel, presumably formed by trajectories similar to those shown in Fig. 6 but on a higher energy potential energy surface. The displaced energetic onset of this channel may result from a barrier along the reaction path. Alternatively, it may be a purely dynamical effect, in the sense that trajectories with just enough energy to reach

the three-body limit could have a higher propensity to drop into one of the $I+I_2$ wells if they deviate at all from the symmetric stretch coordinate.

An interesting question raised by the observation of these channels is the distribution of charge and spin-orbit excitation when three atoms are formed. For channel 4, all we can say is that the probability distribution for the charge must be symmetric, i.e., if P_1 is the probability that the central atom is charged, then $(1-P_1)/2$ is the probability that the charge will be on a particular end atom. For channel 5, the probability distribution for spin-orbit excitation must also be symmetric, with P_2 and $(1-P_2)/2$ the probabilities that the central atom and a particular end atom will be excited, respectively. In addition, the constraint that the charge and spin-orbit excitation cannot be on the same atom means that $P_1+P_2 \leqslant 1$. With our current experimental arrangement, we do not distinguish between charged and neutral photofragments because the charged fragments must be detached in order to be detected, so we cannot determine P_1. However, it should be possible to determine P_1 with other coincidence detector configurations, such as that used by Continetti,[46] and thereby learn more about the three-body dissociation mechanism.

VI. CONCLUSIONS

The work presented here represents the first systematic study of the photodissociation of gas phase I_3^- at multiple dissociation wavelengths. We measured the photofragment yield spectrum of I_3^- and found its maxima at 360 and 290 nm to agree with the two absorption band maxima of I_3^- in solution. Photodissociation dynamics experiments show that I_2^-+I, $I_2^-+I^*$, and I^-+2I are produced at all wavelengths investigated here, and that I^- production occurs via symmetric three-body dissociation.

We hope that these results will stimulate further theoretical work on the I_3^- excited state potential energy surfaces. The observation of I_2^-+I and $I_2^-+I^*$ throughout the PFY spectrum indicates that excitation of either the lower or upper band does not result in adiabatic dissociation to a single asymptote, but instead that complex curve-crossing and nonadiabatic dynamics are present. Our results also show that the differences between the gas phase and short-time solution phase dynamics of I_3^- dissociation exist throughout the absorption bands, not just at the single wavelength (390 nm) investigated previously.

ACKNOWLEDGMENTS

This research is supported by the Director, Office of Energy Research, Office of Basic Energy Sciences, Chemical Sciences Division, of the U.S. Department of Energy under Contract No. DE-AC03-76SP00098.

[1] A. D. Awtrey and R. E. Connick, J. Am. Chem. Soc. **73**, 1842 (1951).
[2] G. C. Pimentel, J. Chem. Phys. **19**, 446 (1951).
[3] W. Gabes and M. A. M. Nijman-Meester, Inorg. Chem. **12**, 589 (1973).
[4] W. Gabes and D. J. Stufkens, Spectrochim. Acta **30A**, 1835 (1974).
[5] P. W. Tasker, Mol. Phys. **33**, 511 (1977).
[6] M. Mizuno, J. Tanaka, and I. Harada, J. Phys. Chem. **85**, 1789 (1981).
[7] T. Okada and J. Hata, Mol. Phys. **43**, 1151 (1981).
[8] M. Isci and W. R. Mason, Inorg. Chem. **24**, 271 (1985).
[9] J. C. Roy, W. H. Hanillm, and R. R. Williams, Jr., J. Am. Chem. Soc. **77**, 2953 (1955).
[10] L. I. Grossweiner and M. S. Matheson, J. Phys. Chem. **61**, 1089 (1957).
[11] A. Barkatt and M. Ottolenghi, Mol. Photochem. **6**, 253 (1974).
[12] K. Kaya, N. Mikami, Y. Udagawa, and T. Ito, Chem. Phys. Lett. **16**, 151 (1972).
[13] W. Kiefer and H. J. Bernstein, Chem. Phys. Lett. **16**, 5 (1972).
[14] A. E. Johnson and A. B. Myers, J. Chem. Phys. **102**, 3519 (1995).
[15] U. Banin, A. Waldman, and S. Ruhman, J. Chem. Phys. **96**, 2416 (1992).
[16] U. Banin and S. Ruhman, J. Chem. Phys. **98**, 4391 (1993).
[17] U. Banin, R. Kosloff, and S. Ruhman, Isr. J. Chem. **33**, 141 (1993).
[18] U. Banin, A. Bartana, S. Ruhman, and R. Kosloff, J. Chem. Phys. **101**, 8461 (1994).
[19] U. Banin, R. Kosloff, and S. Ruhman, Chem. Phys. **183**, 289 (1994).
[20] U. Banin and S. Ruhman, J. Chem. Phys. **99**, 9318 (1993).
[21] T. Kuhne and P. Vohringer, J. Chem. Phys. **105**, 10788 (1996).
[22] T. Kuhne, R. Kuster, and P. Vohringer, Chem. Phys. **233**, 161 (1998).
[23] T. Kuhne and P. Vohringer, J. Phys. Chem. A **102**, 4177 (1998).
[24] K. Do, T. P. Klein, C. A. Pommerening, and L. S. Sunderlin, J. Am. Soc. Mass Spectrom. **8**, 688 (1997).
[25] T. R. Taylor, K. R. Asmis, M. T. Zanni, and D. M. Neumark, J. Chem. Phys. **110**, 7607 (1999).
[26] M. T. Zanni, B. J. Greenblatt, A. V. Davis, and D. M. Neumark, Proc. SPIE **3271**, 196 (1998).
[27] M. T. Zanni, B. J. Greenblatt, A. V. Davis, and D. M. Neumark, J. Chem. Phys. **111**, 2991 (1999).
[28] A. Sanov, T. Sanford, L. J. Butler, J. Vala, R. Kosloff, and W. C. Lineberger, J. Phys. Chem. A **103**, 10244 (1999).
[29] D. R. Cyr, R. E. Continetti, R. B. Metz, D. L. Osborn, and D. M. Neumark, J. Chem. Phys. **97**, 4937 (1992).
[30] R. E. Continetti, D. R. Cyr, R. B. Metz, and D. M. Neumark, Chem. Phys. Lett. **182**, 406 (1991).
[31] D. L. Osborn, D. J. Leahy, D. R. Cyr, and D. M. Neumark, J. Chem. Phys. **104**, 5026 (1996).
[32] D. Hanstorp and M. Gustafsson, J. Phys. B **25**, 1773 (1992).
[33] M. T. Zanni, T. R. Taylor, B. J. Greenblatt, B. Soep, and D. M. Neumark, J. Chem. Phys. **107**, 7613 (1997).
[34] K. P. Huber and G. Herzberg, *Molecular Spectra and Molecular Structure. IV. Constants of Diatomic Molecules* (Van Nostrand Reinhold, New York, 1979).
[35] R. S. Mulliken, J. Chem. Phys. **55**, 288 (1971).
[36] M. T. Zanni, V. S. Batista, B. J. Greenblatt, W. H. Miller, and D. M. Neumark, J. Chem. Phys. **110**, 3748 (1999).
[37] J. Faeder, N. Delaney, P. E. Malsen, and R. Parson, Chem. Phys. Lett. **270**, 196 (1997).
[38] I. Benjamin, U. Banin, and S. Ruhman, J. Chem. Phys. **98**, 8337 (1993).
[39] D. G. Truhlar and J. T. Muckerman, in *Atom-Molecule Collision Theory—A Guide for the Experimentalist*, edited by R. B. Bernstein (Plenum, New York, 1979).
[40] S. K. Kim and D. R. Herschbach, Faraday Discuss. Chem. Soc. **84**, 159 (1987).
[41] Z. H. Wang, T. Wasserman, E. Gershgoren, J. Vala, R. Kosloff, and S. Ruhman, Chem. Phys. Lett. **313**, 155 (1999).
[42] H. L. Friedman, J. Chem. Phys. **79**, 2063 (1953).
[43] D. Meyerstein and A. Treinin, Trans. Faraday Soc. **485**, 1114 (1963).
[44] P. E. Maslen, J. Faeder, and R. Parson, Chem. Phys. Lett. **263**, 63 (1996).
[45] M. T. Zanni, V. S. Batista, B. J. Greenblatt, W. H. Miller, and D. M. Neumark, J. Chem. Phys. **110**, 3748 (1999).
[46] R. E. Continetti, Int. Rev. Phys. Chem. **17**, 227 (1998).